IEEE Access
Multidisciplinary ⋮ Rapid Review ⋮ Open Access Journal

Received 10 November 2025, accepted 24 November 2025, date of publication 27 November 2025, date of current version 4 December 2025.

Digital Object Identifier 10.1109/ACCESS.2025.3638162

RESEARCH ARTICLE

Design of a Novel Flat Cycloidal-Planetary Series Reducer and Experimental Assessment for Assistive Exoskeletons Actuation-CYPLO

RICCARDO BEZZINI, GIULIA BASSANI, CARLO ALBERTO AVIZZANO, AND ALESSANDRO FILIPPESCHI
Institute of Mechanical Intelligence, Scuola Superiore Sant'Anna, 56127 Pisa, Italy
Department of Excellence in Robotics and AI, Scuola Superiore Sant'Anna, 56127 Pisa, Italy

Corresponding author: Riccardo Bezzini (riccardo.bezzini@santannapisa.it)

This work was supported in part by the BRIEF ''Biorobotics Research and Innovation Engineering Facilities'' Project through the National Recovery and Resilience Plan (NRRP), Mission 4 Component 2 Investment 3.1 of the Italian Ministry of University and Research funded by the European Union–NextGenerationEU under Project IR0000036; and in part by the Department of Excellence in Robotics and AI, funded by the Ministry of Research and University under Grant DM 230/2022.

ABSTRACT The recent advancements in assistive exoskeletons have highlighted their effectiveness in reducing the users' metabolic consumption, providing functional compensation, and preventing biomechanical overloads. The exoskeletons' transmission mechanisms are essential for guaranteeing their effectiveness, safety, and comfort. Therefore, lightweight, efficient, backdriveable, and minimally bulky reduction gearboxes with low mechanical output impedance have become a widespread choice in modular assistive exoskeletons. In previous works, the value of the cycloid-planetary series transmission has been assessed. However, the previous design turned out to be too bulky in the axial direction. In this paper, we propose a novel CYcloidal-PLanetary cOncentric series combination (CYPLO) that exploits a compact-cam cycloidal architecture nested inside the sun of a planetary stage. This design enables valuable performance regarding key gearbox features such as regularity, friction, and gear play, while maintaining an extremely advantageous compactness in the axial direction and significant backdriveability even for high transmission ratios. A reducer implementing this novel solution has been designed, developed through 3D printing, and examined experimentally to evaluate its performance with respect to the previous designs and state-of-the-art gearboxes employed in wearable devices' actuators. The results show that this transmission architecture represents a valid solution for lightweight assistive exoskeletons, allowing for high reduction ratios while maintaining compactness and backdriveability.

INDEX TERMS Cycloidal, planetary, gearbox, 3D-print, exoskeletons, actuation, assistance.

I. INTRODUCTION

In recent years, wearable exoskeletons have emerged as a promising solution to enhance human motor functions in diverse domains [1]. These systems are increasingly integrated into occupational environments to mitigate musculoskeletal stress [2], used in clinical rehabilitation to facilitate recovery of motor functions [3], [4], and are employed as assistive devices to support people with limited mobility in performing daily tasks [5], [6]. These wearable systems are designed to facilitate human motion and alleviate the biomechanical loads during multiple tasks while guaranteeing a safe and ergonomic physical Human-Robot Interaction (pHRI) [7]. In the development of wearable exoskeletons, the choice of the transmission or reduction systems plays a key role in determining the actuator's performance, such as torque output, back-drivability, energy efficiency, and form factor, all of which are fundamental to ensuring safe, effective, and ergonomic assistance to the user [8]. Indeed, the central requirement in the actuation of wearable

The associate editor coordinating the review of this manuscript and approving it for publication was Yangmin Li.

robots, particularly in assistive exoskeletons, is the design of efficient, backdriveable, and lightweight actuators that provide sufficient torque while limiting encumbrances and maintaining low output impedance [9]. These attributes are essential not only to ensure user comfort and safety but also to enable intuitive control strategies, allowing the wearers to remain in charge of their motion during assisted walking, thus guaranteeing transparency [10].

Several actuation technologies have been investigated to meet these demands [11]. Among the existing alternatives, spanning from hydraulically actuated exoskeletons [12] to pneumatic [13], from the literature, the paradigm that includes an electric motor and a reduction system emerges as the most popular option [14], [15]. Implementations of this actuation criterion range from quasi-direct drive actuators [16], [17] to designs that implement higher transmission ratios [18]. The choice of the proper reduction gearbox among the existing solutions attempts to find a balance between torque density, mechanical efficiency, and back-drivability, albeit often at the expense of increased encumbrance, complexity, and cost [19].

Within the broad domain of compact speed reducers suitable for wearable exoskeletons actuation, cycloidal [20] and planetary [21] transmissions have been studied both independently and combined into hybrid architectures such as the RV reducers [22]. Cycloidal drives are known for their high torque output, compactness, and smooth contact dynamics, which enable superior load distribution and shock resistance. However, traditional cycloidal mechanisms tend to suffer from large radial dimensions [23]. On the other hand, planetary gear systems offer efficient power transmission in a coaxial form factor but are limited to implementing lower reduction ratios [24]. In previous work [25], the design resulting from the integration of these two architectures in a Cycloidal-Planetary Series combination (CP) demonstrated promising performance in backdriveability, friction, and mechanical robustness. However, since the two reducers' stages were stacked in series, that attempt displayed considerable drawbacks in weight, cost, and axial encumbrance, particularly for applications in wearable assistive devices.

To address these limitations, this work introduces a novel Flat CYcloidal-PLanetary cOncentric architecture (CYPLO), conceived explicitly for exoskeletons' actuation. The key advantage lies in embedding a compact-cam-based [25], [26], [27] cycloidal stage within the sun of a planetary gearbox, thereby achieving a nested, integrated transmission system that significantly reduces axial encumbrances, aiming for an advantageous form factor for assistive wearable devices. Moreover, this design enables a substantial reduction in component count and overall weight (thanks to the employment of a compact-cam architecture for the cycloidal stage) while providing a considerable back-drivability even for high reduction ratios. The novel CYPLO reducer could be proficiently employed for actuator modules in hip and knee joints of assistive lower-limb exoskeletons, enabling

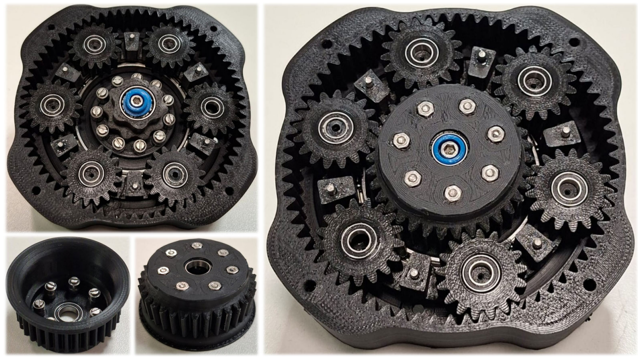

FIGURE 1. Photos of the prototype implementing the presented CYPLO architecture. Starting from the left, in the upper part of the figure, the ring, lower carrier, and planets of the planetary stage are represented, assembled around the first Compact-cam cycloidal stage. The latter includes the first set of rollers, the eccentric shaft, and the compact-cam double disk. The two images in the lower left part present the two views of the same component, that is to say, the sun of the planetary stage and the moving cycloidal base, which contains the rollers for the second stage of the compact-cam architecture. Finally, on the right, the photo illustrates how the cycloidal compact-cam stage is included in the planetary design. The upper part of the planetary carrier was not assembled to clearly display the inner parts of the mechanism.

the employment of high reduction ratios without giving up key features such as compactness and backdriveability. Some photos of the prototype implementing the CYPLO architecture that has been employed for an experimental evaluation of the proposed architecture's performance are reported in Figure 1, where the nested concentric combination of the compact-cam cycloidal and the external planetary stages is displayed. Previous research has explored cycloidal-based nested designs such as the Three-Stage Cycloidal Nested gearbox (TSCN) from [28], which addresses the form factor-ratio limitations of traditional cycloidal mechanisms, proposing a nested architecture for improving the power density of the resulting reducer. However, being based solely on the cycloidal working principle, high-ratio implementations of the TSCN require a high number of rollers (or rolling elements) to meet the torque requirements, thus influencing the transmission's encumbrance, weight, and cost. Moreover, the TSCN design does not guarantee adequate performance in terms of backdrivability.

To present a comprehensive evaluation of the proposed design, this study assesses the reducer's performance regarding key features for transmission systems, such as friction, backdriveability, gear play, stiffness, and regularity. The presented metrics are then evaluated and discussed regarding the employment of the presented device in wearable robotics applications.

The main contributions of this paper are the following:

- The definition of a novel flat concentric cycloidal-planetary transmission architecture that integrates a Compact-Cam cycloidal phase within a planetary reduction stage. This design, conceived for compact and efficient integration in wearable assistive devices, enables high transmission ratios while guaranteeing significant backdriveability and compactness.

- The design of a 3D-printed prototype implementing a 1:52.5 reduction ratio. In addition to the CAD files and bill of materials of the presented prototype, an executable tool (and its source Python code) for the geometric design of a custom CYPLO reduction gearbox is available at [29].
- The experimental assessment of the presented prototype, evaluated both with respect to other state-of-the-art gearboxes (including the previous Cycloidal-Planetary series transmissions from [25]) and to validate its use in an actuation module for assistive exoskeletons.

The remainder of this paper is organized as follows: Section II presents the design and implementation of the novel Nested Flat Cycloidal-Planetary reducer architecture, then describing the setup and methodology employed for the experimental assessment. Section III reports and discusses the results of the performance evaluation. Finally, Section IV concludes the paper and suggests directions for future research in the development of lightweight transmission systems for human-centered robotics.

II. MATERIALS AND METHODS

A. BACKGROUND

Before presenting the novel CYPLO combination, brief descriptions of the compact-cam cycloidal architecture and the epicyclic planetary design are depicted.

1) CYCLOIDAL COMPACT-CAM DESIGN

The compact-cam cycloidal architecture has been developed to further miniaturize gearboxes without sacrificing the reduction ratio [26]. This configuration simplifies the classical mechanism by employing a single eccentric crankshaft and a pair of rigidly connected cycloidal disks, thus deleting the need for a carrier. This allows for the implementation of high reduction ratios in a compact radial form.

Given the Cycloidal Compact-cam stage reduction ratio:

$$i = \frac{n_1 \, Nr_2}{n_1 \, Nr_2 - n_2 \, Nr_1}, \tag{1}$$

n_i denotes the number of disk lobes at the i^{th} stage and N_{ri} represents the number of rollers at the i^{th} stage. For designing the CYPLO prototype, the employed cycloidal profiles were defined such that $n_i = Nr_i - 1$.

The main limitation of this architecture consists of the restrictive relation between the number and dimensions of the rollers, the eccentricity, the torque capacity, and the resulting backdriveability. Despite allowing for high transmission ratios with a limited number of rollers in the two stages and a lower mechanical complexity (the cycloidal carrier is not included in this design), the output torque capabilities are restricted by the eccentricity and the number of rollers: indeed, disks with low eccentricities and few rollers are not capable of exerting high torques. Nonetheless, increasing the number of rollers and the eccentricity hinders the reducer's simplicity (increasing weight, cost, and volume) and severely impacts the resulting backdriveability, as confirmed by the results presented in our previous work [25] about the evaluated compact-cam prototypes.

2) EPICYCLIC PLANETARY STAGE

Planetary transmissions have four main components: the sun gear, planetary gears, the carrier, and the ring gear, which is the only internally toothed component of the reducer. This kind of mechanism comprehends several modes of operation, determined by which parts are fixed and which parts rotate. Typically, only two of the three sets of gears will rotate. Concerning the implementations presented in this work, the planetary configuration consists of a fixed ring gear, a rotating sun gear as the input, and a rotating carrier (connected to the planet gears) as the output.

The gear ratio in a planetary transmission is determined by the difference in the number of teeth on the ring gear and the sun gear. Given the following equations, which represent the sun–planet and planet–ring interactions, respectively, the overall gear ratio of a planetary gearbox can be deduced in the generic case, which involves the rotation of the gears:

$$N_s\omega_s + N_p\omega_p - (N_s + N_p)\omega_c = 0 \tag{2}$$

$$N_r\omega_r + N_p\omega_p - (N_r + N_p)\omega_c = 0 \tag{3}$$

where N stands for the number of teeth, ω represents the rotating velocity, and the subscripts s, p, r, and c denote *sun*, *planet*, *ring*, and *carrier*, respectively. Concerning the planetary gear sets presented in this work, we consider the relation between the number of teeth:

$$N_r = N_s + 2N_p. \tag{4}$$

Moreover, as mentioned previously, the ring gear is fixed in the designed gearboxes, so $\omega_r = 0$. Finally, the transmission ratio considered here for the single-stage planetary transmissions is as follows:

$$\frac{\omega_c}{\omega_s} = \frac{N_s}{N_s + N_r}. \tag{5}$$

Usually, simple epicyclic planetary stages used with a stationary ring gear are used for implementing gear ratios that vary from 1:3 to 1:9, which displays a clear limitation if the target ratio is higher, forcing to resort to complex compound architectures or multiple planetary stages. Moreover, the higher the desired ratio, the bigger the planets have to be with respect to the sun, highly impacting the reducer's volume and weight.

B. CYPLO ARCHITECTURE

This study presents a novel transmission system conceived for wearable exoskeleton applications, improving the previous hybrid Cycloidal-Planetary reducer architecture by embedding a compact-cam cycloidal stage into the sun of a planetary gearbox. The core novelty of this architecture lies in its spatial integration strategy: the cycloidal reduction stage is embedded concentrically within the Sun gear of the planetary stage, significantly reducing axial length without compromising mechanical performance. In this novel configuration, the output of the compact-cam gearbox and the sun gear (i.e., the input of the planetary stage) are actually the same component. This design represents an evolution of the previous Cycloidal-Planetary configuration [25], aiming for the maintenance of the previously established significant features while improving compactness even for high reduction ratios, an essential characteristic for wearable devices' actuators.

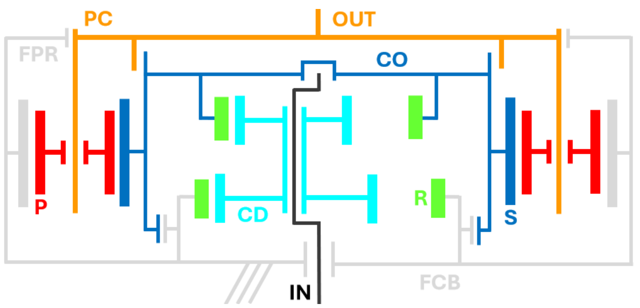

FIGURE 2. Schematic illustration of the structure of the cycloidal-planetary CYPLO series reducer. The acronyms reported are abbreviations for the parts illustrated with the same color. IN refers to the input shaft (in black) with a single eccentric section. FCB refers to the fixed cycloidal base (in light grey), to which the rollers (R, in light green) are connected. CD refers to the compact-cam cycloidal disk. CC refers to the cycloidal carrier (depicted in blue), which is also the planetary Sun, S. P stands for planet (in red), while FPR refers to the fixed planetary ring, which is rigidly connected to the cycloidal base. PC refers to the planetary carrier that corresponds to the output of this reducer.

To overcome these limitations, the novel design implements a flat, nested configuration, wherein the cycloidal stage occupies the internal volume of the Sun gear. This nesting not only reduces the total axial dimension but also allows for a decrease in overall mass and component count, thanks to the substitution of the classic cycloidal stage with the compact-cam architecture. Indeed, traditional cycloidal reducers display high radial encumbrances. A schematic cross-sectional illustration of the proposed architecture is reported in Figure 2, where all the components are represented in different colors to facilitate the comprehension of the design. This spatially efficient layout enables higher gear ratios to be implemented without increasing the gearbox encumbrance, a critical factor for applications demanding unobtrusive wearability. Moreover, unlike other architectures (such as the harmonic drive) that allow for high transmission ratios while maintaining a flattened shape, the CYPLO design, through the series combination of a cycloidal and a planetary stage, is supposed to guarantee significant backdriveability and low output impedance for improved transparency and user comfort in wearable robotics applications.

To sum up, this design aims at combining the high-ratio capacity and low mechanical complexity (leading to low weight and low encumbrance) of the compact-cam cycloidal design with the high torque capability of spur gears, which, on the other hand, are limited in transmission ratio, as explained previously. Including one stage inside the other and employing a single component both as the sun of the planetary stage and the moving base of the compact-cam reducer drastically reduces the axial encumbrance, whose limit is actually imposed by the choice of the rollers and bearings employed. As the nested architecture poses some strict constraints on the design of the two stages of the presented architecture, we provide a straightforward tool for supporting the geometric design choices during the development of a CYPLO reducer.

1) CYPLO GEOMETRIC DESIGN TOOL

To facilitate and encourage the exploration and analysis of the proposed nested cycloidal-planetary architecture, we provide an executable tool and its source code at [29] for the geometric definition of a custom CYPLO reducer. Starting from the user's definition of the desired outer planetary stage ratio and maximum radial encumbrance, the proposed instrument first asks the user for the desired gear module. Then, given the previously gathered information, the tool presents all the possible combinations of teth numbers (and possible equivalently distant planet gears) to obtain the target i (see equation 5). Once the planetary stage has been defined, given that the cycloidal stage is contained in the sun gear (which will be the compact-cam output), a radial constraint is defined for the encumbrance of the compact-cam stages. The user then inserts the diameter of the rollers that should be used. Based on this feature and given the sun dimensions, the maximum number of rollers that can be employed for a cycloidal stage is defined and employed to compute all the possible combinations of the number of rollers for the two stages N_1 and N_2 that can produce the compact-cam desired reduction ratio, The remaining parameters (E, D_1, D_2) for the cycloidal profile delineation are requested (and checked base on the mentioned restrictions). At this point, a compact-cam geometry is arranged. After defining the necessary geometrical variables, the resulting cycloidal profiles and set of rollers are displayed through sketches, allowing the user to review their choices and optionally adjust some parameters. Once all the selected variables are confirmed, two figures show the resulting view of the two cycloidal stages contained in the planetary sun gear (for simplicity, the sun, ring, and planets are represented through circles with a diameter equal to the primitive circles of the gears).

The resulting CYPLO gearbox has a combined reduction ratio of:

$$i_{TOT} = \frac{N_s n_1 \, Nr_2}{(N_s + N_r)(n_1 \, Nr_2 - n_2 \, Nr_1)} \tag{6}$$

C. 3D-PRINTED PROTOTYPE

1) DESIGN ASSUMPTIONS AND CONSTRAINTS

The final goal regarding the CYPLO prototype's volume and weight was to strongly decrease the previous CP30 and CP80 axial encumbrance to provide a transmission whose form factor converged to a flat shape. Since the previous

Cycloidal-Planetary reducers from [25] were composed by stacking the two stages in the axial direction, their radial encumbrance resulted in a quite low value (78 mm diameter). With the CYPLO architecture, we do not aim at limiting the reducer's horizontal expansion, as a flat form actually fits the needs in most wearable assistive devices, reducing the overall augmentation of the user volume while wearing the exoskeleton. Therefore, based on previous results and state-of-the-art standards, we set the prototype limits at 90 mm for the diameter and 35 mm for the axial encumbrance. Regarding the target ratio, we aimed for a value between the ones explored in our previous work for a fair comparison with both the previous prototypes. Moreover, given the aim of employing the resulting device in exoskeletons, a reasonable target appeared to be around 1:50, implemented in multiple wearable devices [30], [31], [32].

TABLE 1. Design parameters of the presented CYPLO 3D-printed prototype.

Symbol	Value	Description
i_{pl}	1 : 3	Planetary stage Reduction Ratio
z_r	68	Number of teeth Ring
z_{pa}	17	Number of teeth Planets
N_p	6	Number of Planets
z_{sa}	34	Number of teeth Sun
α	25°	Teeth pressure angle
m	1.2 mm	Teeth Module
R_c	30.6 mm	Planetary Carrier Radius
i_{cy}	1 : 17.5	Cycloidal stage Reduction Ratio
D_{pr1}	29 mm	Rollers Pitch Diameter (Stage 1)
N_{r1}	11	Number of rollers (Stage 1)
D_{pr2}	24 mm	Rollers Pitch Diameter (Stage 2)
N_{r2}	7	Number of rollers (Stage 2)
D_r	5 mm	Roller Diameter
E	1 mm	Eccentricity

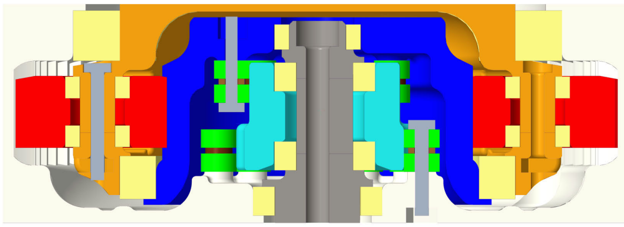

(a) Front section CAD view of the presented CYPLO prototype.

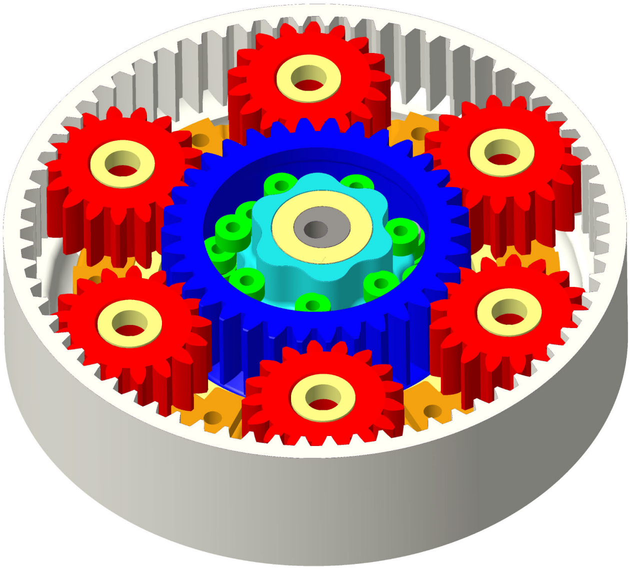

(b) Top section CAD view of the presented CYPLO prototype. The top parts of the carrier and base are not included to give a view of the internal mechanism.

FIGURE 3. CAD section views of the CYPLO prototype. The colors employed match the ones in Figure 2. The view presented in Figure 3(b) is similar to the one illustrated in the photos from Figure 1. The fixed cycloidal base and the fixed planetary ring are depicted in light grey. The input shaft with the eccentric cam is in dark grey. The bearings employed as rollers in the cycloidal stage are illustrated in light green, while the structural bearings are yellow. The compact cam cycloidal disk is turquoise. The moving cycloidal base (that is also the sun of the planetary stage) is displayed in blue. The planet gears are red, while the planetary carrier (which is also the whole reducer's output) is orange.

2) GEARBOX DESIGN AND PARAMETERS

Employing the procedure implemented in the available CYPLO tool (and aiming for low weights in the choice of bearings), the resulting device's design parameters were chosen. Their values are reported in Table 1. The designed reducer achieves a total gear ratio of 1:52.5. This ratio ensures sufficient torque amplification from compact electric motors while maintaining low impedance and responsiveness in backdrive scenarios, critical for safety and compliance in human-exoskeleton interaction. The gear ratio is achieved through the two-stage cycloidal-planetary combination: the compact-cam cycloidal stage contributes a ratio of 1:17.5, while the planetary stage adds a subsequent 1:3 multiplication, resulting in a compact 1:52.5 overall reduction. As the goal ratio was set to 1:50 (with a ± 3 tolerance, which is needed as the cycloidal compact-cam architecture has not only precise resulting ratios), the planetary set was kept as limited in dimensions as possible. Indeed, with the blocked ring and input sun, the ratio rises only by increasing the planets' teeth (as the sun dimension cannot be decreased excessively since it should contain the cycloidal stage). The selected teeth distribution was employed because it allowed for an equally spaced distribution of a high number of planets (6), according to the rule:

$$\frac{N_s + N_r}{n_p} = I \quad (7)$$

where n_p represents the number of planets and $I \in \mathbb{Z}$. Consequently, the internal compact-cam stage implements a quite low ratio (considering the possibilities given by the design itself), included between 1:15.67 and 1:17.67 (considering the previously mentioned tolerance). The chosen number of rollers and eccentricity were the result of a trade-off between a reasonable torque capacity (which demands for high number of rollers and eccentricity) and a low backdrive torque (that on the contrary, gets higher with the eccentricity). Two CAD section views of the resulting prototype are reported in Figure 3, employing the same colors used in the Figure 2 for the displayed components to facilitate the interpretation of the parts.

3) MATERIALS, PRINTERS, AND COMPONENTS

To develop the CYPLO prototype, Ultimaker PLA and Ultimaker Nylon12-CF have been employed, given their valuable combination of low costs and significant mechanical properties [33], [34]. More precisely, PLA has been employed for the shaft and the gears that compose the planetary stage, while Nylon12CF has been used for the compact-cam cycloidal disk and the planetary carrier, i.e., the reducer's output. The manufacturing process involved the use of the Ultimaker S7 Pro Bundle and the Ultimaker Method XL printers, with slicing carried out via Ultimaker Cura. The parts that were not produced through 3D printing were the bearings, screws, and nuts. The bill of materials and CAD files of the presented prototypes are available at [29], together with the executable geometric design tool and its source Python code.

D. EXPERIMENTAL EVALUATION

In this section, the experimental setup employed to evaluate the chosen metrics is described. Then, the selected performance metrics are presented, together with the respective experimental protocols defined for evaluating the CYPLO prototype with respect to different Cycloidal-Planetary Series combinations and other garboxes.

1) TEST BENCH SETUP

The experimental setup is composed of a brushless motor (EC 90 flat, 360 W, *phi*90 mm, Maxon, Bad Homburg, Germany), which includes an integrated 2-channel encoder (MILE 512–6400 CPT, Maxon) coupled to the reducer's input shaft through the 3D-printed motor support. The reducer's output component is connected to an incremental magnetic encoder (H2 Series, Phoenix America, Fort Wayne, IN, USA) that is fixed to the support structure through a 3D-printed part. All the mentioned components are fixed to horizontal aluminum beams through a 3D-printed support structure. The motor-encoder assembly is controlled by a three-phase brushless DC motor driver (STEVAL-SPIN3201, STMicroelectronics, Geneva, Switzerland). The magnetic encoder and the two load cells (CZL635, Phidgets Inc.), which can be placed in a case on the output arm if the test demands the force detection at the reducer's output, are connected to the STM32 Nucleo-144 board (NUCLEO-F767ZI, STMicroelectronics). Both these boards are connected to the central unit (Intel NUC 11 Pro, i7-1165G7) running Windows 11 and Simulink (MATLAB, Mathworks Inc., Natick, MA, USA), where a PID controller (*discrete PID controller,* Simulink block) is designed to manage the motor's speed, depending on the performed test. A custom Kalman filter (*Matlab function,* Simulink block) is employed to estimate the motor speed to be employed as a feedback for the velocity control. The registered data in the output log files for the performed tests includes the motor's position, estimated speed, and current, the load cells' force signal, the reference control signal, the base timer, and the magnetic encoder reading for the reducer's output position.

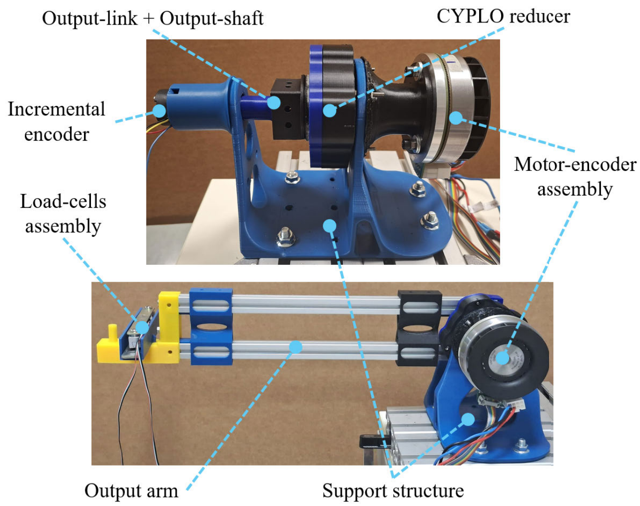

FIGURE 4. Experimental setup employed for testing the CYPLO prototype. The two photos and the notes clarify the composition of the experimental setup, both in the configuration with and without the output arm and the load cells.

Figure 4 displays the setup with photos of the two exploited experimental arrangements, where the main components are illustrated and pointed out. As can be noted from these figures, one configuration does not involve the use of the output arm, since the tests conducted in this arrangement did not include output forces or torques measurements. The output arm is composed of two 20 × 20mm aluminum beams held together with 3D-printed parts, which also include the terminal elements that can be coupled with the load cells assembly components.

2) EVALUATION METRICS AND PROTOCOLS

To evaluate the CYPLO prototype's performance (and compare it with the previous design from [25]), the following metrics have been taken into consideration. For each analyzed metric, the experimental protocol is explained.

a: FRICTION

Represents the torque that the motor has to exert to counteract static (Coulomb) and dynamic (viscous) resistances opposing reducer motion. Quantifying internal friction is critical for applying compensation strategies, which in turn improve actuator transparency in pHRI.

The motor's internal static and viscous friction were identified by commanding the motor to track multiple slowly-ramping speed references. The resulting current measurements were used to identify and fit a friction model for a proper compensation. For each experiment, six velocity ramp signals have been employed: three for positive and three for negative speeds. The reference signals were built to ramp from 0 to ±100 rad/s, following the methodology reported in [35], with low accelerations of 0.1, 0.2, and 0.3 rad/s^2. Each test was executed three times for the proposed prototype. Given the results obtained in [25] for the other printed gearboxes, at first, speed and torque data were employed to fit the following asymmetric friction model:

$$\tau_{fr} = \begin{cases} M_c^+ + d_v^+ \omega_m, & \text{if } \omega_m \geq 0, \\ -M_c^- + d_v^- \omega_m, & \text{if } \omega_m \leq 0, \end{cases} \tag{8}$$

where τ_{fr} denotes the friction torque, M_c^+ and M_c^- the Coulomb friction components (respectively for positive and negative velocities), d_v^+ and d_v^- the viscous coefficients, and ω_m the motor speed.

However, the recorded data were not compatible with the model presented in Equation (8). Thus, we resorted to the more detailed Stribeck friction curve, modeled according to the following equation:

$$\tau_{fr} = \sqrt{2e}\,(M_{brk} - M_c)\, e^{-\left(\frac{\omega}{\omega_{st}}\right)^2} \frac{\omega}{\omega_{st}} + M_c \tanh\left(\frac{\omega}{\omega_{coul}}\right) + d\omega, \tag{9}$$

with the characteristic velocities defined as

$$\omega_{st} = \omega_{brk}\sqrt{2}, \qquad \omega_{coul} = \frac{\omega_{brk}}{10}, \tag{10}$$

where $M(v)$ is the friction Moment as a function of the relative velocity v, M_{brk} is the breakaway (stiction) friction force, M_c is the Coulomb friction force, ω_{st} is the Stribeck velocity threshold, ω_{coul} is the Coulomb friction threshold velocity, ω_{brk} is the breakaway velocity, d is the viscous friction coefficient. All the mentioned velocities (referred to as ω) refer to the motor speed. This model captures the nonlinear decay of friction from the breakaway value M_{brk} toward the Coulomb level M_c as velocity increases, with ω_{st} shaping the Stribeck effect. At higher velocities, the viscous term d becomes dominant, resulting in a linear growth of friction. The presented model's parameters were identified by fitting the experimental data using MATLAB's *lsqcurvefit* nonlinear least-squares optimization function, which minimizes the squared error between the measured data and the model prediction. The suitability of the fitting procedure was assessed through the evaluation of the coefficient of determination R^2, to ensure the reliability and statistical robustness of the parameters' estimation.

b: SPEED REGULARITY

Refers to the oscillatory deviation between the measured reducer output speed and its theoretical value, which is computed as the product of the motor angular velocity and the transmission ratio. This value represents the expected reducer's output motion in ideal conditions, providing insight about the stability and accuracy of speed transmission, as this feature depends on the effects of the transmission error (TE). This value is defined as the deviation between the actual gearbox output angle and the expected output angle [36]:

$$TE = \theta_{out} - i\theta_{in}, \tag{11}$$

where TE is the transmission error, θ_{out} the measured output angle, θ_{in} the motor input angle, and i the nominal reduction ratio. Building on the TE definition, the regularity metric quantifies the deviation between the actual reducer's output speed and its theoretical value, providing a measure of the actuator's capability to track a precise velocity. A PID controller was employed to regulate the motor speed according to a sequence of step inputs ranging from 0 to ± 120 rad/s in increments of 20 rad/s, according to the procedure employed in previous work [25], so that the CYPLO prototype's regularity could be compared fairly with the other Cycloida-Planetary reducers. Each test was repeated three times for both positive and negative velocities.

Regularity as a percentage value was then computed according to the formula:

$$R = 100\left(1 - \frac{\Delta\omega_g}{i\,\omega_m}\right), \tag{12}$$

where R denotes the regularity (expressed as %), ω_g is the measured gearbox's output speed, i represents the reduction ratio, and ω_m the motor speed.

c: GEAR PLAY

This metric is defined as the output angular range of motion that is observed with the motor input shaft locked, thus a condition in which no resisting torque is transmitted from the actuator. A smaller gear play reflects higher positional accuracy in motion transmission.

The gear play was quantified by measuring the maximum output displacement while keeping the motor's shaft (thus the reducer's input) blocked. To avoid the effect of joint stiffness, the procedure consisted of manually moving the reducer's output link without applying significant torque. The measurement was repeated at i (i.e., the reducer's transmission ratio) consecutive motor positions, evenly spaced by an entire 360° motor rotation completed manually, to characterize the backlash over one full revolution of the reducer's output, aiming for a complete evaluation of gear play in a high number of internal positions for the gearbox's mechanism. The CYPLO prototype's gear play was tested in three different sections to ensure consistency of the results.

d: GEAR STIFFNESS

The CYPLO prototype's stiffness can be defined as the ratio between the applied torque at the output link (with the motor input shaft locked) and the resulting angular displacement. This metric is relevant since higher stiffness enhances tracking accuracy in trajectory-control tasks, whereas lower stiffness provides compliance, beneficial for smoother and safer physical human-robot interaction (pHRI).

The experimental setup for testing gear stiffness involved the use of the output arm equipped with the load cell assembly, mounted with a lever arm length of 0.43 m. Transmission stiffness was identified by manually applying a series of increasing loads to the arm end (directly on the load cells) while recording the load-cell force signal. The applied loads allow for testing the transmission stiffness up to 35 Nm at the output (this value also includes the torque contribution due to the weight of the arm and load cells assembly). Testing the prototype up to this target torque allows for an evaluation within a set of plausible values for wearable assistive exoskeletons such as [37] and [38].

Each test was repeated three times per reducer, with output positions incremented by 60° to capture possible position-dependent variations. The resulting torque-displacement data were employed to fit a linear model to estimate the output stiffness, defined as:

$$k_g = \frac{\Delta \tau_{out}}{\Delta \theta_{out}}, \tag{13}$$

where k_g denotes the CYPLO transmission stiffness, $\Delta\tau_{out}$ is the applied torque at the output arm, and $\Delta\theta_{out}$ is the corresponding angular displacement registered through the incremental encoder. For each loading process (from 0 Nm to 30-35 Nm), the mean stiffness has been computed. Then, the mean value and standard deviation for each reducer have been computed. As for the friction model fitting, the experimental data from the stiffness tests were employed to minimize the squared error with respect to the model prediction by MATLAB's *lsqcurvefit* function. The accuracy of the fitting process was assessed using the coefficient of determination (R^2) to confirm the reliability and statistical soundness of the estimated parameters.

e: BACKDRIVE TORQUE

The torque that must be applied to the output link through the arm to initiate motor motion. This feature is influenced by the inertia of the motor assembled with the reducer. This characteristic is particularly relevant in actuators for wearable exoskeletons, which must not hinder the user's voluntary movements. The more a reducer displays backdrivability, the easier it is for the wearer to initiate motion without feeling high undesired interaction forces [7], [39], [40].

The experimental setup to identify the CYPLO prototype backdrive torque included both the output arm and the load cells, whose weight is included in the computation of the overall applied torque. At the beginning of each test, the motor was positioned such that the output arm remained horizontal, providing a reference to correctly account for the torque contribution of the arm and load weight, which varied with the angular configuration. Forces were manually applied to the load cells in increasing magnitude until motor displacement was observed. Each test was performed at least five times and repeated in three independent sessions. Backdrive torque was then estimated by identifying motor displacement — detected using a threshold of 0.18°, which is twice the motor encoder resolution - and calculating the corresponding applied torque considering the load cells data, the arm weight, and its angular position with respect to the horizontal reference in which the experiment is initiated. The mean value is computed based on all the performed experiments, to account for potential differences depending on the internal conditions of the gearbox.

f: SIZE, WEIGHT, AND COST

The reducers were fabricated using Ultimaker PLA (polylactic acid) and Ultimaker Nylon12-CarbonFiber, so the overall mass, bulk, and cost depend on the proportion in which PLA and NY12CF are employed, and the quantity and type of bearings and fasteners employed. Reducing mass and bulk is essential in wearable robotics to enhance usability and user acceptance. Moreover, achieving low production costs without compromising mechanical performance is fundamental to facilitating the widespread deployment of assistive technologies.

Regarding the prototypes' encumbrance, the maximum height and diameter of the reducers were first derived from the CAD models and then verified through physical measurements. The presented encumbrances report the gearboxes' shapes without considering the connection with the employed setup, implemented through four screws on a ϕ70 mm circumference to connect the motor support and the reducer to the printed support. Therefore, the comparison between the encumbrances does not depend on the experimental setup, but only on the prototypes' design, so that a fair comparison, even with other gearboxes from the literature, can be conducted.

The overall cost was estimated by summing the price of the non-printed components (e.g., bearings, screws, and nuts) with the cost of the 3D-printed parts. The cost of the PLA and N12CF elements was determined based on their weight, accounting for the material price, the energy consumption during fabrication, and the amortization of the printers over their expected lifetime. For the non-printed components, prices were obtained from the supplier's catalog and scaled according to the quantities employed for the CYPLO prototype. Finally, the total mass of each reducer was measured directly using a precision scale.

III. RESULTS AND DISCUSSION

The torque (current) and velocity data from one of the friction tests, together with the respective friction model fit, are illustrated in Figure 5. From the reported data, it is clear how the Stribeck model was necessary for an accurate

TABLE 2. Results from the friction tests. For the CP30 and CP80 reducers from [25], the Coulomb static friction has been employed as a reference breakaway value.

ID	Breakaway Friction [mNm]	Coulomb Friction [mNm]	Viscous Factor [mNms/rad]
CP30 [25]	**13.4 ± 0.39**	**13.4 ± 0.39**	$1.16 \pm 0.09 \cdot 10^{-1}$
CP80 [25]	13.7 ± 0.75	13.7 ± 0.75	$1.59 \pm 0.1 \cdot 10^{-1}$
CYPLO	57.2 ± 1.83	26.1 ± 0.99	$\mathbf{0.145 \pm 0.021} \cdot 10^{-1}$

TABLE 3. Results from the tests regarding Gear Play, Gear Stiffness, and Backdrive Torque. The best value for each feature is reported in bold.

ID	Gear Play [°]	Gear Stiffness [Nm/rad]	Backdrive Torque [Nm]
CP30 [25]	1.1 ± 0.14	573.6 ± 59.52	**0.59 ± 0.03**
CP80 [25]	0.89 ± 0.23	472.5 ± 43.15	0.70 ± 0.04
CYPLO	**0.175 ± 0.053**	**859.56 ± 55.62**	1.08 ± 0.07

description of the gearbox internal friction. The values employed for the Stribeck friction model describing the CYPLO prototype behavior are reported in Table 2, together with the parameters of the two Cycloidal-Planetary reducers from [25]. The friction characterization achieved an R^2 value of 0.88, demonstrating a high degree of consistency between the empirical data and the obtained model. It should be noted that, for a fair comparison, the CP30 and CP80 parameters have been adapted to the Stribeck friction model, employing the original Coulomb static variable for the Breakaway value. The static friction presents higher values with respect to the CP30 and CP80 devices, mainly due to the fact that during the design of this prototype, lower tolerances were employed to improve the poor gear play feature identified in the other two Cycloidal-Planetary reducers, leading to slightly more difficult assembly. However, despite being higher than the CP30 and CP80 values, the static friction in the CYPLO prototype is still significantly lower with respect to other gearboxes [35], [41]. From the reported data, it is clear that the proposed prototype shows a remarkably low viscous friction component, as it is also confirmed by Figure 5, where the friction rises only minimally with the velocity. The 0.145 ± 0.021 10^{-1} value results notably negligible value, especially considering other state-of-the-art printed and metal-built gearboxes such as the ones from [25], [35], and [41], where the lowest viscous coefficient reported is 3.57 10^{-5} Nms/rad. Therefore, the nested combination of the two stages emerges as a valuable solution, since no increase of motor torque (i.e., motor current) is required at higher velocities, thus not reducing the actuator's torque capacity at higher speeds.

Concerning the backdrive torque, the discussed increase in internal friction inevitably induces a higher torque required to initiate the motor motion from the gearbox's output side. Nevertheless, the computed 1.08 Nm backdrive torque still represents a highly viable solution for wearable devices. Indeed, not only is this value lower than the one registered for other reducers employed on wearable exoskeletons [16], [41], but it is also a negligible quantity with respect to the

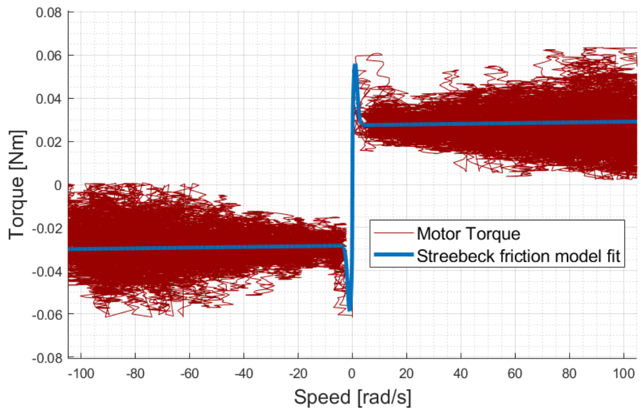

FIGURE 5. Example of data from one of the performed friction tests. The motor torque is plotted with respect to the velocity. Also, the Stribeck fitted model for the specific experiment is illustrated.

reducer's torque capacity (35 Nm), consisting of just 3 % of the allowed output torque.

As mentioned before, lower tolerances with respect to our previous work [25] (which negatively influenced the static breakaway and coulomb friction) were adopted to improve the CP30 and CP80 gear plays (respectively, 1.1° and 0.89°). As reported in the Table 3, the CYPLO prototype exhibits a substantial gear play reduction of approximately 80–85% compared to the other devices, indicating a substantial improvement, and proving to be better than the 3D-printed cycloidal reducers from [23] and [35].

Regarding the gearbox stiffness, it is worth noting that multiple details in the design and manufacturing of the presented prototype aimed at improving the reducer's rigidity: the use of Nylon12CarbonFiber for the cycloidal compact-cam disk, the bigger module for the planetary gears and the higher number of planets with respect to the CP30 and CP80 prototypes, and the use of steel pins for reinforcing the planetary carrier's rigidity. Given these features, as confirmed by the values reported in Table 3, the CYPLO prototype displays a significant increase in stiffness, reaching a value of 859.6 ± 55.6 Nm/rad. This result indicates a highly reduced elastic deformation under torque, contributing to enhanced control precision and dynamic responsiveness and thus confirming the effectiveness of the proposed architecture in minimizing mechanical compliance. The linear regression model used to characterize the stiffness reached an R^2 value of 0.81, indicating a strong correspondence between the experimental measurements and the fitted trend. The resulting CYPLO stiffness is also higher than the values estimated for all the reducers from our previous work [25].

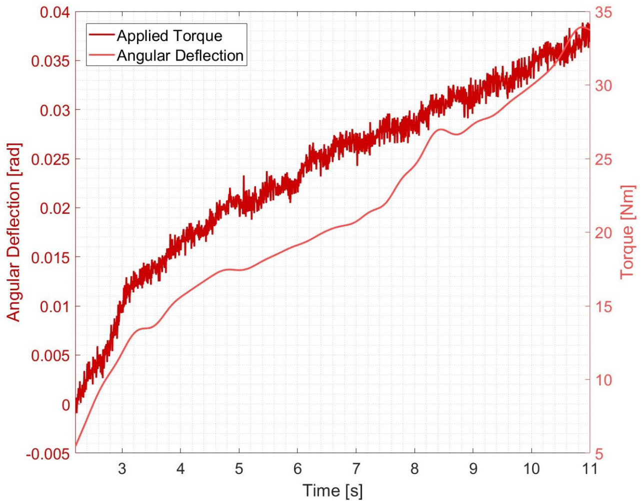

FIGURE 6. Example of data from one of the performed Stiffness tests during one of the three loading conditions. The applied torque (right y-axis) and the output angular deflection (left y-axis) are illustrated with respect to time.

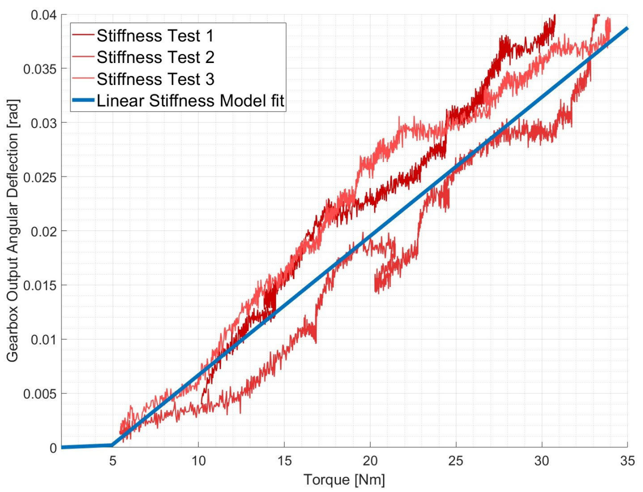

FIGURE 7. Example of data from one of the performed Stiffness tests. The applied torque on the gearbox output is plotted with respect to the angular deflection. The red lines represent the three loading phases of the considered test. The blue line represents the stiffness model fitted through the gathered torque-deflection data.

As a more direct demonstration of the resulting stiffness, Figure 6 illustrates the applied torque and resulting angular deflection during one of the loading phases of a stiffness test. From this image, the linear relation between torque and deflection is quite evident. The same goes for the data presented in Figure 7, where data from a complete stiffness test (including three loading phases) are reported, illustrating the output angular displacement with respect to the applied torque and the fitted linear stiffness model. The three loading phases demonstrate a fairly similar behavior.

Concerning the speed regularity of the presented CYPLO prototype, the results for all the investigated motor velocities and the total regularity value are reported in the Table 4, where the best values among the CP30, CP80, and CYPLO prototypes are highlighted in bold characters. The three considered reducers demonstrated consistently high motion regularity across the entire speed range, with mean values above 95%, indicating a relatively smooth and stable torque transmission with acceptable transmission errors. Among them, the CYPLO prototype achieved the highest average regularity (96.23 ± 0.34 %), outperforming the previous Cycloidal-Planetary prototypes. These results confirm that the choices regarding the compact-cam stage eccentricity for the proposed design effectively keep the kinematic irregularities, typically associated with backlash and transmission non-linearities, at a valuable level. This is confirmed by the fact that these values are better than all the regularities computed for the other cycloidal-based reducers analyzed in our previous work [25]. Such valuable behavior is particularly advantageous for wearable and assistive robotic systems, where velocity smoothness directly influences user comfort and control accuracy. Also, the similarity of the regularity values for the different velocities demonstrates promising stability for wearable robotics applications.

The sizes (maximum diameter and height), weights, and costs of the CYPLO prototype are reported in Table 5, together with the data from [25] for the CP30 and CP80 gearboxes. The best values are written in bold characters.

Regarding the cost, the low number of bearings needed for the compact-cam design with respect to a classical cycloidal stage benefits the overall price, which results in a reduction of roughly 16–26% in cost. The overall cost surely confirms the CYPLO design as a beneficial solution for cost-effective gearboxes.

Concerning the height, the novel nested cycloidal-planetary concentric series configuration proved itself worthy, providing an upper limit on the axial encumbrance independently of the reduction ratio. The 30.25 m height proved to be substantially lower with respect to all eight reducers presented in [25], and even with reference to other 3D-printed and metal-built gearboxes [16], [42], [43]. Clearly, the flat design could increase in diameter depending on the choices regarding the cycloidal and planetary stages, as explained in the previous section. Anyway, this particular CYPLO prototype shows quite a low radial encumbrance, especially given the reduction ratio. Other gearboxes display higher encumbrances, even when implementing lower transmission ratios [35].

TABLE 4. Regularity of the reducers at the investigated motor velocities.

Motor Speed [rad/s]	20	40	60	80	100	120	R_{TOT}
CP30 [25] Regularity [%]	95.5	94.8	95.77	95.85	94.87	**96.25**	95.51 ± 0.57
CP80 [25] Regularity [%]	95.9	**96.88**	94.9	94.35	95.51	95.68	95.54 ± 0.87
CYPLO Regularity [%]	**96.86**	95.65	**96.29**	**96.48**	**96.51**	96.03	**96.23 ± 0.34**

TABLE 5. Encumbrances (maximum diameter and height), weight, and cost of the presented reducers.

ID	Diameter [mm]	Height [mm]	Weight [g]	Cost [€]
CP30 [25]	**78**	52	272	116.26
CP80 [25]	**78**	52	302	131.42
CYPLO	87	**30.45**	**271**	**97.05**

Considering the weight, which is a key feature for reducers in exoskeletons, as it allows for lighter wearable devices that result in more comfortable and easier-to-use devices, the CYPLO prototype shows lower mass with respect to both the CP30 and CP80 gearboxes. As for the price, the use of a compact-cam cycloidal stage instead of a classical one strongly reduces the number of components and thus the reducer's weight. Indeed, the proposed reducer displays a remarkably lower mass with respect to other gearboxes [16], [35], [42]. Taking as a reference the data reported in the scoping review from [44] regarding the reducers employed in exoskeletons, the overall CYPLO mass results well below the lower presented weights of the analyzed transmissions.

A. OVERALL CONSIDERATIONS

The results confirmed that the CYPLO architecture substantially not only outperforms previous Cycloidal-Planetary designs (CP30 and CP80), but also surpasses other state-of-the-art 3D-printed and metal-built reducers for wearable robotics. In particular, the CYPLO prototype achieved an 80-85% reduction in gear play with respect to CP30 and CP80 and a ≈50% increase in stiffness (859.6 ± 55.6 Nm /rad) reaching a valid robustness for the range of torque of the intended application. The proposed design also improved speed regularity (96.23 ± 0.34%), and maintained a low back-drive torque (≈1 Nm, corresponding to ≈3% of rated output torque). These performance improvements are achieved while maintaining a flat geometry (30.45 mm height), a low mass (271 g), and a reduced cost (97x20AC;), confirming the effectiveness of the compact nested configuration. The reduced axial size enables seamless integration into existing wearable actuation modules without compromising torque capability, while the lower friction, high regularity, and enhanced stiffness support more transparent and accurate assistance during physical human–robot interaction.

IV. CONCLUSION

This work presented the design of a novel nested Cycloidal-Planetary Concentric architecture for gearboxes conceived to enhance the actuation of assistive exoskeletons, allowing for flat, compact, and lightweight reducers even for high transmission ratios, accompanied by the realization and experimental characterization of a CYPLO 3D-printed prototype. Motivated by the limitations of existing gearboxes, often constrained by excessive axial encumbrance, limited stiffness, low backdriveability, and high cost, the proposed approach combines a cycloidal compact-cam stage within a planetary stage, achieving high reduction ratios within a flat and lightweight configuration.

A comprehensive experimental assessment of the 3D-printed 52.5:1 prototype was carried out to assess its frictional behavior, speed regularity, stiffness, gear play, and backdrivability, following validated evaluation protocols and therefore allowing for a fair comparison with previous Cycloidal-Planetary designs and state-of-the-art gearboxes. The collected results demonstrate that CYPLO reducers represent a promising class of transmissions for assistive exoskeletons, balancing efficiency, compactness, regularity, and significant performance for all the analyzed metrics. The modular architecture can be adapted to diverse joint configurations, enabling the development of lightweight and cost-effective assistive actuators. To encourage the use of this architecture, a geometric design tool is provided, together with the CAD files of the tested prototype.

Future work will focus on fabricating metal versions of the CYPLO reducer to further increase load capacity, optimizing the geometry to minimize encumbrances in smaller-scale variants, and integrating the transmission into a functional exoskeleton to assess its performance in real human-assistance tasks. Moreover, the presented design tool will be enhanced to include in the design process considerations based on theoretical models to provide the users with insights regarding the reducer's performance based on the selected design parameters.

REFERENCES

[1] C. Siviy, L. M. Baker, B. T. Quinlivan, F. Porciuncula, K. Swaminathan, L. N. Awad, and C. J. Walsh, "Opportunities and challenges in the development of exoskeletons for locomotor assistance," *Nature Biomed. Eng.*, vol. 7, no. 4, pp. 456–472, Dec. 2022.

[2] S. Crea, P. Beckerle, M. De Looze, K. De Pauw, L. Grazi, T. Kermavnar, J. Masood, L. W. O'Sullivan, I. Pacifico, C. Rodriguez-Guerrero, N. Vitiello, D. Ristic-Durrant, and J. Veneman, "Occupational exoskeletons: A roadmap toward large-scale adoption. Methodology and challenges of bringing exoskeletons to workplaces," *Wearable Technol.*, vol. 2, p. e11, 2021.

[3] A. Plaza, M. Hernandez, G. Puyuelo, E. Garces, and E. Garcia, "Wearable rehabilitation exoskeletons of the lower limb: Analysis of versatility and adaptability," *Disab. Rehabil., Assistive Technol.*, vol. 18, no. 4, pp. 392–406, May 2023.

[4] L. Luo, Z. Wei, Y. Sun, W. Zhang, and J. Zhou, "Preliminary design and control of an ankle rehabilitation robot with variable stiffness actuator," *IEEE Access*, vol. 12, pp. 195906–195917, 2024.

[5] S. Qiu, Z. Pei, C. Wang, and Z. Tang, "Systematic review on wearable lower extremity robotic exoskeletons for assisted locomotion," *J. Bionic Eng.*, vol. 20, no. 2, pp. 436–469, Mar. 2023.

[6] A. Aljarah, M. I. Awad, M. Boushaki, and I. Hussain, "Design optimization of a variable stiffness actuator for knee exoskeleton application," *IEEE Access*, vol. 11, pp. 52740–52749, 2023.

[7] R. Bezzini, C. A. Avizzano, F. Porcini, and A. Filippeschi, "Transparency evaluation for the kinematic design of the harnesses through human-exoskeleton interaction modeling," in *Proc. IEEE/RSJ Int. Conf. Intell. Robots Syst. (IROS)*, Oct. 2024, pp. 9335–9341.

[8] B. Laschowski and J. McPhee, "Energy-efficient actuator design principles for robotic leg prostheses and exoskeletons: A review of series elasticity and backdrivability," *J. Comput. Nonlinear Dyn.*, vol. 18, no. 6, Jun. 2023, Art. no. 060801.

[9] A. Calanca, S. Toxiri, D. Costanzi, E. Sartori, R. Vicario, T. Poliero, C. D. Natali, D. G. Caldwell, P. Fiorini, and J. Ortiz, "Actuation selection for assistive exoskeletons: Matching capabilities to task requirements," *IEEE Trans. Neural Syst. Rehabil. Eng.*, vol. 28, no. 9, pp. 2053–2062, Sep. 2020.

[10] E. Mobedi and M. I. Can Dede, "A continuously variable transmission-based variable stiffness actuator for pHRI: Design optimization and performance verification," *J. Mech. Robot.*, vol. 16, no. 8, Aug. 2024, Art. no. 081013.

[11] M. Tiboni, A. Borboni, F. Vérité, C. Bregoli, and C. Amici, "Sensors and actuation technologies in exoskeletons: A review," *Sensors*, vol. 22, no. 3, p. 884, Jan. 2022.

[12] W. Fan, Z. Dai, B. Zhang, L. He, M. Pan, J. Yi, and T. Liu, "HyExo: A novel quasi-passive hydraulic exoskeleton for load-carrying augmentation," *IEEE/ASME Trans. Mechatronics*, vol. 30, no. 1, pp. 144–155, Feb. 2025.

[13] L. Mišković, M. Dežman, and T. Petrič, "Pneumatic exoskeleton joint with a self-supporting air tank and stiffness modulation: Design, modeling, and experimental evaluation," *IEEE/ASME Trans. Mechatronics*, vol. 29, no. 5, pp. 3415–3426, Oct. 2024.

[14] Y. Xia, W. Wei, X. Lin, and J. Li, "Optimization of torque-control model for quasi-direct-drive knee exoskeleton robots based on regression forecasting," *Sensors*, vol. 24, no. 5, p. 1505, Feb. 2024.

[15] D. Rodríguez-Jorge, S. Zhang, J. S. Huang, I. Lopez-Sanchez, N. Srinivasan, Q. Zhang, X. Zhou, and H. Su, "Biomechanics-informed mechatronics design of comfort-centered portable hip exoskeleton: Actuator, wearable interface, controller," *IEEE Trans. Med. Robot. Bionics*, vol. 7, no. 2, pp. 687–698, May 2025.

[16] S. Yu, T.-H. Huang, X. Yang, C. Jiao, J. Yang, Y. Chen, J. Yi, and H. Su, "Quasi-direct drive actuation for a lightweight hip exoskeleton with high backdrivability and high bandwidth," *IEEE/ASME Trans. Mechatronics*, vol. 25, no. 4, pp. 1794–1802, Aug. 2020.

[17] T.-H. Huang, S. Zhang, S. Yu, M. K. MacLean, J. Zhu, A. Di Lallo, C. Jiao, T. C. Bulea, M. Zheng, and H. Su, "Modeling and stiffness-based continuous torque control of lightweight quasi-direct-drive knee exoskeletons for versatile walking assistance," *IEEE Trans. Robot.*, vol. 38, no. 3, pp. 1442–1459, Jun. 2022.

[18] Y. Zhang, M. Bressel, S. De Groof, F. Dominé, L. Labey, and L. Peyrodie, "Design and control of a size-adjustable pediatric lower-limb exoskeleton based on weight shift," *IEEE Access*, vol. 11, pp. 6372–6384, 2023.

[19] P. L. García, S. Crispel, E. Saerens, T. Verstraten, and D. Lefeber, "Compact gearboxes for modern robotics: A review," *Frontiers Robot. AI*, vol. 7, p. 103, Aug. 2020.

[20] C. Barsomian, N. B. P. Eswaran, M. Pesenti, M. Gandolla, F. Braghin, E. Carpanzano, and L. Roveda, "Dynamic characterization and control of a back-support exoskeleton 3D-printed cycloidal actuator," *CIRP Ann.*, vol. 73, no. 1, pp. 29–32, 2024.

[21] B. Jenks, H. Levan, and F. Stefanovic, "OpenSEA: A 3D printed planetary gear series elastic actuator for a compliant elbow joint exoskeleton," *Frontiers Robot. AI*, vol. 12, Feb. 2025, Art. no. 1528266.

[22] Y. Zhao, Z. Han, Q. Tan, W. Shan, R. Li, H. Wang, and Y. Du, "Multi-objective optimization design of cycloid-pin gears based on RV reducer precision transmission performance," *Energies*, vol. 17, no. 3, p. 654, Jan. 2024.

[23] W. Roozing and G. Roozing, "3D-printable low-reduction cycloidal gearing for robotics," in *Proc. IEEE/RSJ Int. Conf. Intell. Robots Syst. (IROS)*, Oct. 2022, pp. 1929–1935.

[24] H. Matsuki, K. Nagano, and Y. Fujimoto, "Bilateral drive gear—A highly backdrivable reduction gearbox for robotic actuators," *IEEE/ASME Trans. Mechatronics*, vol. 24, no. 6, pp. 2661–2673, Jun. 2019.

[25] R. Bezzini, G. Bassani, C. A. Avizzano, and A. Filippeschi, "Design and experimental evaluation of multiple 3D-printed reduction gearboxes for wearable exoskeletons," *Robotics*, vol. 13, no. 11, p. 168, Nov. 2024.

[26] T.-C. Lin, M. Schabacker, Y.-L. Ho, T.-C. Kuo, and D.-M. Tsay, "Geometric design and dynamic analysis of a compact cam reducer," *Machines*, vol. 10, no. 10, p. 955, Oct. 2022.

[27] H. Yang, Y. Li, J. Huang, X. Li, and L. Sun, "Theoretical analysis and performance prediction of a nn-type precision cycloidal reducer," *Forschung im Ingenieurwesen*, vol. 88, no. 1, p. 44, 2024.

[28] L. Maccioni, F. Concli, and M. Blagojevic, "A new three-stage gearbox concept for high reduction ratios: Use of a nested-cycloidal architecture to increase the power density," *Mechanism Mach. Theory*, vol. 181, Mar. 2023, Art. no. 105203.

[29] R. Bezzini. (2025). *Cycc-PLA-Gearbox: Cycloidal-Planetary Gearbox Geometric Design and CAD Files*. [Online]. Available: https://github.com/RicBez/CYCC-PLA-gearbox

[30] A. Calanca, E. Dimo, E. Palazzi, and L. Luzi, "Enhancing force controllability by mechanics in exoskeleton design," *Mechatronics*, vol. 86, Oct. 2022, Art. no. 102867.

[31] E. Palazzi, L. Luzi, E. Dimo, M. Meneghetti, R. Vicario, R. F. Luzia, R. Vertechy, and A. Calanca, "An affordable upper-limb exoskeleton concept for rehabilitation applications," *Technologies*, vol. 10, no. 1, p. 22, Jan. 2022.

[32] J. Qiu, L. Dong, R. Guo, Y. He, H. Cheng, and W. Li, "Multi-terrain adaptive control for knee exoskeletons: Development and experimental evaluation," in *Proc. China Autom. Congr. (CAC)*, Nov. 2024, pp. 1658–1663.

[33] I. Buj-Corral and E. E. Zayas-Figueras, "Comparative study about dimensional accuracy and form errors of FFF printed spur gears using PLA and nylon," *Polym. Test.*, vol. 117, Jan. 2023, Art. no. 107862.

[34] R. Ciobanu, G. Arhip, O. Dontu, C. I. Rizescu, and B. Gramescu, "Additive manufacturing meets gear mechanics: Understanding abrasive wear evolution in FDM-printed gears," *Polymers*, vol. 17, no. 13, p. 1810, Jun. 2025.

[35] W. Roozing and G. Roozing, "Experimental comparison of pinwheel and non-pinwheel designs of 3D-printed cycloidal gearing for robotics," in *Proc. IEEE Int. Conf. Robot. Autom. (ICRA)*, May 2024, pp. 7091–7098.

[36] H. Xu, Z. Shi, B. Yu, and H. Wang, "Optimal measurement speed and its determination method in the transmission precision evaluation of precision reducers," *Appl. Sci.*, vol. 9, no. 10, p. 2146, May 2019.

[37] O. Kang, J. Yun, S. Seo, H.-M. Joe, H. Yi, and S. Lee, "A novel design of unpowered exoskeleton for loaded walking using only hip abduction torque," *IEEE/ASME Trans. Mechatronics*, vol. 29, no. 4, pp. 2534–2544, Aug. 2024.

[38] S. Luo, M. Jiang, S. Zhang, J. Zhu, S. Yu, I. Dominguez Silva, T. Wang, E. Rouse, B. Zhou, H. Yuk, X. Zhou, and H. Su, "Experiment-free exoskeleton assistance via learning in simulation," *Nature*, vol. 630, no. 8016, pp. 353–359, Jun. 2024.

[39] F. Yi, C. Zhang, S. Chen, S. Qiu, H. Zhang, Q. Du, W. Wang, and G. Yang, "A compact actuator for lower-limb exoskeletons with high torque density and high backdrivability," *IEEE/ASME Trans. Mechatronics*, early access, Aug. 13, 2025, doi: 10.1109/TMECH.2025.3593993.

[40] S. Zhao, K. Walters, J. M. Pérez, and R. D. Gregg, "Design and validation of a modular, backdrivable ankle exoskeleton," in *Proc. 10th IEEE RAS/EMBS Int. Conf. Biomed. Robot. Biomechatronics (BioRob)*, Sep. 2024, pp. 1454–1460.

[41] J. Seiler, N. Schäfer, G. Zhao, B. Latsch, M. Grimmer, P. Beckerle, and M. Kupnik, "Human-exoskeleton interaction force estimation based on quasi-direct drive actuators," in *Proc. 10th IEEE RAS/EMBS Int. Conf. Biomed. Robot. Biomechatronics (BioRob)*, Sep. 2024, pp. 1132–1139.

[42] T. Yoshida, G. Endo, A. Okubo, and H. Nabae, "Experimental evaluation of a quasi-direct-drive actuator with a 3D-printed planetary gear reducer," in *Proc. IEEE/SICE Int. Symp. Syst. Integr. (SII)*, Jan. 2023, pp. 1–6.

[43] S. Hur, D. Kim, C. Lee, and D. Choi, "Optimal design of a compound planetary reducer using a nonlinear optimization method," *IEEE Access*, vol. 11, pp. 7822–7828, 2023.

[44] F. Bettella, S. Tortora, E. Menegatti, N. Petrone, and A. Del Felice, "A scoping review on lower limb exoskeleton actuation's description and characteristics," *Robotica*, vol. 43, no. 4, pp. 1–18, Mar. 2025.

RICCARDO BEZZINI received the B.S. degree in mechanical engineering from the University of Florence, Italy, in 2019, and the M.S. degree (Hons.) in robotics and automation engineering from the University of Pisa, Italy, in 2023. He is currently pursuing the Ph.D. degree in emerging digital technologies (perceptual robotics) with the Institute of Mechanical Intelligence, Scuola Superiore Sant'Anna, Pisa, Italy. His research interests include human–robot interaction modeling, biomechanical analysis, exoskeletons' design, and the development of gearboxes and actuation systems for wearable robotics applications.

GIULIA BASSANI received the M.S. degree in biomedical engineering from the University of Pisa, in 2012, and the Ph.D. degree in emerging digital technologies from Scuola Superiore Sant'Anna (SSSA), in 2017. She is currently a Research Fellow with the Mechanical Intelligent Institute, SSSA. She participated in national and industrial projects aimed at the automatic assessment of the biomechanical overload risk with a wearable sensor network. She contributed to the Foresight and Technology Injection-H12023 and the EU Exosmooth projects. Her main research interests include sEMG acquisition and processing, human body motion acquisition and analysis, wearable sensor networks, estimation of ergonomic risk, embedded wearable energy harvesting systems, and deep learning.

CARLO ALBERTO AVIZZANO received the B.S. degree in control and automation from the University of Pisa, in 1995, and the Ph.D. degree in robotics, in 1999. He is currently the Director of the Intelligent Automation System Laboratory and the Coordinator of the Department of Excellence in Robotics and Artificial Intelligence, Scuola Superiore Sant'Anna, Pisa, Italy. His skills include control, robotics, computer vision, artificial intelligence, mechatronics, embedded systems, and haptics. He has been cooperating in EU, National, Regional, and Industrial projects, since 1996. To date, he is the owner of about 15 industrial patents and has authored more than 170 scientific and peer-reviewed papers in journals and conference proceedings. His research interests include intelligent sensing and control systems, industry 4.0, smart wearable devices, human–robot interfaces with high cognitive capabilities, autonomous vehicles, and drones in cognitive-aware high-perception tasks.

ALESSANDRO FILIPPESCHI received the M.S. degree in mechanical engineering from the University of Pisa, in 2007, and the Ph.D. degree in perceptual robotics from Scuola Superiore Sant'Anna, in 2012. He is currently an Assistant Professor of applied mechanics with Scuola Superiore Sant'Anna. He participated in more than 20 national and EU projects. His research interests include the capture and analysis of human motion, estimation of the ergonomic risks, and the development of exoskeletons and haptic interfaces for human–robot interaction. He is a Co-Founder of Wearable Robotics.